The vertical Fermi and eROSITA bubbles inclined jets: A proof-of-concept study

Po-Hsun Tseng [ID],[1] H.-Y. Karen Yang [ID],[2] Hsi-Yu Schive [ID],[1, 3, 4, 5] and Tzihong Chiueh [ID][1, 3, 4]

[1]*Institute of Astrophysics, National Taiwan University, Taipei 10617, Taiwan*
[2]*Institute of Astronomy and Department of Physics, National Tsing Hua University, Hsinchu 30013, Taiwan*
[3]*Department of Physics, National Taiwan University, Taipei 10617, Taiwan*
[4]*Center for Theoretical Physics, National Taiwan University, Taipei 10617, Taiwan*
[5]*Physics Division, National Center for Theoretical Sciences, Taipei 10617, Taiwan*

ABSTRACT

1. Release the caveat of jet direction.

2. Rule out the hadronic process.

3. Predict the small inner bubbles.

4. How to explain why we assume e_CR ■ e_gas

5. How to explain the lifespan of bubbles is too long.

6. How to explain the jet power.

7. How to explain the inconsistant of gamma-ray map.

Keywords: keywords

1. INTRODUCTION

2. METHODOLOGY

We used the GPU-accelerated special relativistic hydrodynamics AMR code (GAMER-SR) developed at the National Taiwan University (Schive et al. 2010, 2018; Tseng et al. 2021) to carry out the simulations of the Fermi and eROSITA bubbles by CR and relativistic fluid injections from the GC.

The CRs are advected with the thermal gas, and in return the velocities of gas can react to the gradients of the CR pressure via the source term containing spatial divergence of fluid velocities.

Although the high-energy CRe (10 — 100 GeV) plays a crucial role in reproducing the γ-ray map within the range of 1 — 100 GeV, we assume the pressure of CRe is much less than that of gas throughout the simulation so that we , and the Fermi bubbles can be outlined against the eROSITA bubbles.

Corresponding author: Po-Hsun Tseng
zengbs@gmail.com

As stressed by Yang et al. (2012), CR diffusion has insignificant effect on the overall morphology of the Fermi bubbles, but only sharpens the edges of the simulated bubbles by the interplay between anisotropic CR diffusion and magnetic fields with suppressed perpendicular diffusion across the bubble surface. Moreover, the bubbles should be weak due to adiabatic expansion, and thus the magnetic fields has little effect on the overall dynamics. For these two reasons, we have ignored the CR diffusion and the magnetic field throughout the simulation.

We do not simulate the spectral evolution of the CR, and we neglected the cooling and heating processes of CRs, such as energy losses due to synchrotron and inverse Compton emission, and reacceleration in shocks.

In this approach, we treat CRs as a single species without distinction between electrons and protons, that cannot react to the gas via the application of CRe pressure, and solve directly for the evolution of CR energy density e_{cr} as a function of $\mathbf{r}$ and t.

Since the relativistic fluid ejected by the jet source is quickly stalled off and slowed down by a dense ISM

disk in a short time, and the relativistic fluid accounts for a little minority of total mass inside the simulation box, we still use the Newtonian gravity to attack this problem.

The governing equations solving the special relativistic ideal fluid including CR advection, and dynamical coupling between the thermal gas and CRs without CR diffusion turn out to be

$$\partial_t D + \partial_j \left(D U^j / \gamma \right) = 0, \tag{1a}$$

$$\partial_t M^i + \partial_j \left(M^i U^j / \gamma + p_{\text{gas}} \delta^{ij} \right) = -\rho \partial_t \Phi, \tag{1b}$$

$$\partial_t \tilde{E} + \partial_j \left[\left(\tilde{E} + p_{\text{gas}} \right) U^j / \gamma \right] = 0, \tag{1c}$$

$$\partial_t \left(\gamma e_{\text{cr}} \right) + \partial_j \left(e_{\text{cr}} U^j \right) = -p_{\text{cr}} \partial_j U^j, \tag{1d}$$

where the five conserved quantities of gas D, M^i, and $\tilde{E}$ are the mass density, the momentum densities, and the reduced energy density, respectively. The reduced energy density is defined by subtracting the rest mass energy density of gas from the total energy density of gas. γ and U^j are the temporal and spatial component of four-velocity of gas. ρ is the gas density in the local rest frame defined by D/γ. p_{gas} is the gas pressure. p_{cr} and e_{cr} are the CR pressure and CR energy density measured in the local rest frame. Φ is the gravitation potential. c is the speed of light, and δ^{ij} is the Kronecker delta notation. Throughout this paper, Latin indices run from 1 to 3, except when stated otherwise.

The set of Equation (1) is closed by using the Taub-Mathews equation of state (Taub 1948; Mathews 1971) that approximates the exact EoS (Synge 1957) for ultra-relativistically hot gases coexisting with non-relativistically cold gases.

GAMER-SR adopts a new algorithm (Tseng et al. 2021) to convert between primitive (ρ, U^j, p) and conserved variables (D, M^j, $\tilde{E}$), significantly reducing numerical error caused by catastrophic cancellations that commonly occur within the regions with high Mach number flows. e.g., jet-ISM interaction zones.

GAMER-SR also adaptively and locally reduce the min-mod coefficient (Tseng et al. 2021) within the failed patch group. Doing so provides an elegant way to avoid the use of pressure/density floor, being unnatural but widely used in almost publicly available codes.

2.1. The Galactic and Disk Models

As a proof-of-concept study, we approximate conventionally axisymmetric stellar potential of Milky Way by an external plane-parallel potential that is symmetric about the mid-plane $z = 0$ in a simulation box size of $14 \times 14 \times 28$ kpc, slightly larger than the size of eROISTA bubbles.

The plane-parallel potential is fixed throughout our simulations and given by

$$\Phi_{\text{total}}(z) = \Phi_{\text{bulge}}(z) + \Phi_{\text{halo}}(z), \tag{2}$$

where

$$\Phi_{\text{bulge}}(z) = 2\sigma_{\text{bulge}}^2 \ln \cosh \left(z \sqrt{\frac{2\pi G \rho_{\text{bulge}}^{\text{peak}}}{\sigma_{\text{bulge}}^2}} \right) \tag{3}$$

is the potential of an isothermal slab mainly contributed by stars around the Galactic bulge, and $\Phi_{\text{halo}}(z) = v_{\text{halo}}^2 \ln \left(z^2 + d_{\text{h}}^2 \right)$ is a plane-parallel dark logarithmic halo potential.

With the help of the isothermal and hydrostatic equilibrium conditions, and assuming the interface between isothermal disk and atmosphere is in pressure equilibrium, we can write the steady-state gaseous density distributions, confined in the total potential, of the disk and the Galactic atmosphere as

$$\rho_{\text{isoDisk}}(z) = \rho_{\text{isoDisk}}^{\text{peak}} \exp \left[-\frac{\Phi_{\text{total}}(z)}{k_B T_{\text{isoDisk}} / m_{\text{p}}} \right] \tag{4a}$$
$$, \text{ if } |z| < z_0$$

$$\rho_{\text{atmp}}(z) = \rho_{\text{atmp}}^{\text{peak}} \exp \left[-\frac{\Phi_{\text{total}}(z)}{k_B T_{\text{atmp}} / m_{\text{p}}} \right] \tag{4b}$$
$$, \text{ otherwise,}$$

where m_{p} is the proton mass, T_{isoDisk} and T_{atmp} is the temperature of the isothermal disk and atmosphere, $\rho_{\text{isoDisk}}^{\text{peak}}$ and $\rho_{\text{atmp}}^{\text{peak}}$ is the peak mass density of the disk and atmosphere on the mid-plane $z = 0$.

We tabulate parameters in the first four categories of Table 1, except for $\rho_{\text{atmp}}^{\text{peak}}$ that can be derived from the known parameters and pressure equilibrium condition on the interfaces ($z = \pm z_0$) between the disk and atmosphere.

The initial density profile of Equation (4) is shown in Figure 1(a) and compared to the observed result (Miller & Bregman 2013) beyond 1 kpc.

Note that there is an difficulty in disentangling the contribution of the Local Bubble, a supernova remnant in which the Solar System is embedded (Snowden et al. 1990), and the contribution from solar wind charge-exchange processes, which produce soft X-ray emission throughout the Solar System. As a result, the density profile of the Galactic halo remains unclear (Bland-Hawthorn & Gerhard 2016).

The AMR base level is covered by $16 \times 16 \times 32$ root grids, refined progressively on the plane $z = 0$, with the outflow boundary condition.
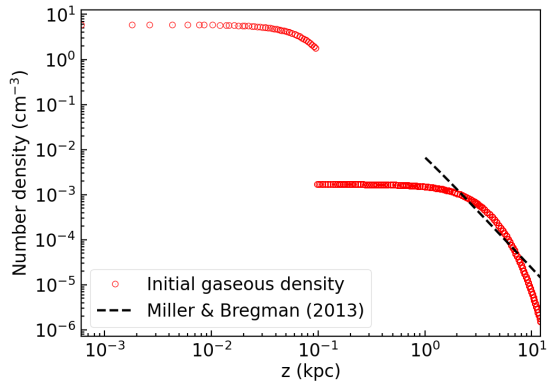
(a) The initial gaseous density profile along z-axis

Figure 1. Captions

2.1.1. *The clumpy, and warm/cold ISM disk*

A crucial component in our work is the clumpy ISM disk initialized by the publicly available pyFC code [1]. First, pyFC create a dimensionless clumpy distribution $f_{\mathrm{clumpy}}(\mathbf{x})$ obeys the log-normal probability distribution with mean μ_{clumpy} and dispersion σ_{clumpy}, and follows the power-law Kolmogorov spectrum

$$D(\mathbf{k}) = \int k^2 \hat{f}(\mathbf{k})\hat{f}^*(\mathbf{k})d\Omega \propto k^{-\beta}, \qquad (5)$$

where $\hat{f}(\mathbf{k})$ is the Fourier transform of $f_{\mathrm{clumpy}}(\mathbf{x})$. The spectrum $D(\mathbf{k})$ in the Fourier space is characterized by the power law index β, the Nyquist limit $k_{\max}$, and the lower cutoff wave number $k_{\min}$. $k_{\max}$ is one-half of the spatial resolution within disk, and $k_{\min}$ is 375.0, corresponding to the maximum size of an individual clump ~ 20 pc.

The temperature in each cell of the clumpy disk is determined by p_{disk}

We summarize the parameters of clumpy disk and their references in Table 1.

Lewis & Austin (2002) and Wagner et al. (2012) have outlined a detailed procedure for constructing clumpy structure, and we do not repeat here.

The temperature in each cell of the warm gas distribution is determined by pressure equilibrium with hot gas. When the warm gas temperature exceeds $T_{\mathrm{crit}} =$ K, it is deemed to be thermally unstable and is replaced by hot gas. This makes the gas porous.

1. Constructing the isothermal disk $\rho_{\mathrm{isoDisk}}(\mathbf{x})$ by Equation (4a).

2. Using PyFC code to obtain a dimensionless clumpy distribution f_{clumpy} obeying lognormal distribution and the power-law spectrum, Equation (5).

3. $\rho_{\mathrm{ismDisk}}(\mathbf{x}) = \mathbf{f}_{\mathrm{clumpy}}(\mathbf{x})\rho_{\mathrm{isoDisk}}(\mathbf{x})$.

4.

1. Assumptions on gravity:

   (a) We use the potential of isothermal slab, symmetric about $z = 0$ and supported by gas pressure and by under its own self-gravity, to mimic the realistic potential of Galactic bulge.

(b) The ISM disk and atmosphere are subjected to the fixed external potential due to a disk bulge and dark matter halo.

(c) In addition to the gravitational interaction, we ignore other interactions between stars and gases.

(d) We also ignore the self-gravity of the ISM disk and of the atmosphere.

(e) We ignore the centrifugal force of Milky Way rotation acting on the bubbles.

(f) We use the potential of isothermal slab to mimic the gravitational potential due to the stellar bulge.

(g) The interface between cold ISM disk and atmosphere is parallel to the Galactic plane and is pressure balanced.

1. Fixed external gravitational potential:

   (a) Bulge potential:

   i. Peak density: $\rho_{\mathrm{bulge}}^{\mathrm{peak}} = 4 \times 10^{-24}$ g/cm^3.

   ii. Potential (isothermal slab):

   $$\Phi_{\mathrm{bulge}} = 2\sigma_{\mathrm{bulge}}^2 \ln\cosh\left(z\sqrt{\frac{2\pi G\rho_{\mathrm{bulge}}^{\mathrm{peak}}}{\sigma_{\mathrm{bulge}}^2}}\right), \tag{6}$$

   where $\sigma_{\mathrm{bulge}} = \sqrt{\dfrac{k_B T_{\mathrm{bulge}}}{m}} = 100$ km/s (Valenti et al. 2018).

   (b) Dark logarithmic halo potential:

   $$\Phi_{\mathrm{halo}} = v_{\mathrm{halo}}^2 \ln\left(z^2 + d_{\mathrm{h}}^2\right), \tag{7}$$

   where $v_{\mathrm{halo}} = 131.5$ km/s, $d_{\mathrm{h}} = 12$ kpc (Yang et al. 2013).

   (c) Total potential: $\Phi_{\mathrm{total}} = \Phi_{\mathrm{bulge}} + \Phi_{\mathrm{halo}}$.

2. Clumpy cold disk:

   (a) Dimension: 14×14×0.2 kpc. i.e. Scale height, $z_0 = 100$ pc. (Ferrière 2001)

   (b) Peak mass density: $\rho_{\mathrm{disk}}^{\mathrm{peak}} = 10^{-23}$ g/cm^3. (Ferrière 2001)

   (c) Average temperature: $T_{\mathrm{disk}} = 10^3$ K. (Ferrière 2001)

   (d) Average mass density:

   $$\rho_{\mathrm{disk}} = \rho_{\mathrm{disk}}^{\mathrm{peak}} \exp\left[-\frac{\Phi_{\mathrm{total}}}{k_B T_{\mathrm{disk}}/m}\right]. \tag{8}$$

   (e) Pressure: $p_{\mathrm{disk}} = \rho_{\mathrm{disk}} T_{\mathrm{disk}}$.

Table 1. Parameters of the disk, atmosphere, and gravitational potential in the simulation.

Parameter	Description	Value
Static stellar potential (Valenti et al. 2018)		
σ_{bulge}	Velocity dispersion of bulge	100 km·s^{-1}
$\rho_{\text{bulge}}^{\text{peak}}$	Peak average density of bulge	4×10^{-24} g·cm^{-3}
Static dark halo potential (Johnston et al. 1995)		
v_{halo}		131.5 km·s^{-1}
d_{h}	Core radius	12 kpc
Isothermal disk (Ferrière 2001)		
z_0	Scale height of disk	100 pc
T_{isoDisk}	Temperature of disk	10^3 K
$\rho_{\text{isoDisk}}^{\text{peak}}$	Peak mass density of disk	10^{-23} g·cm^{-3}
Atmosphere (Tepper-García et al. 2015)		
T_{atmp}	Temperature of atmosphere	10^6 K
Clumpy disk (Wagner et al. 2012)		
T_{c}	Critical temperature of warm atomic phase	3×10^4 K
k_{min}	Cutoff wave number	375.0
μ_{clumpy}	Mean of number density	1.0 cm^{-3}
σ_{clumpy}	Dispersion of number density	1.7 cm^{-3}
β	Power law index	$-5/3$

(f) The clumpy cuboid, using the publicly available pyFC code[2], are described by a log-normal distribution with mean 1.0 and variance 5.0. Also, the power spectrum of the clumpy cuboid is characterized by k_{min} and β, where k_{min} sets the maximum cloud size within the clumpy cuboid, and β is the slope of power spectrum in Fourier space. In this paper, we set $\beta = -5/3$ and $k_{\text{min}} = 375$ to follow the Kolmogorov spectrum and to limits the maximum size of an individual cloud to approximately 25 pc.

(g) The clumpy disk is then constructed by multiplying a fractal cuboid with Equation (8).

(h) The clouds and voids within clumpy disk are pressure balanced.

3. Isothermal atmosphere:

(a) The region outside the clumpy cold disk is atmosphere.

(b) $T_{\text{atmp}} = 10^6$ K. (Tepper-García et al. 2015)

(c) Density:

$$\rho_{\text{atmp}} = \rho_{\text{atmp}}^{\text{peak}} \exp\left[-\frac{\Phi_{\text{total}}}{k_B T_{\text{atmp}}/m}\right], \quad (9)$$

where $\rho_{\text{atmp}}^{\text{peak}}$ can be obtained by assuming that pressure and gravitational potential are continuous at the interface ($z = \pm z_0$) between disk and atmosphere.

2.2. Cold disk

We restrict the refinement level is 7 within the cold disk so that a molecular cloud can be adequately resolved by approximately 30 cells along their diameter, 100 pc.

2.3. Jet injection

We resolve the jet source located at the center of the simulation domain, cells are refined to level 11, leading to a finest spatial resolution of 0.4 pc.

1. Why the overall structure is insensitive to jet direction?

   (a) Jet source size.

   (b) Cold disk.

   (c) Large pressure gradient along z-dircetion.

2.4. X-ray and Gamma-ray emission

1. X-ray:

   (a) Thermal bremsstrahlung: The X-ray emissivity in an energy range 1.4–1.6 keV is calculated using the MEKAL model

(Mewe et al. 1985; Kaastra & Mewe 1993; Liedahl et al. 1995) implemented in the utility XSPEC(Arnaud 1996), assuming solar metallicity.

2. Gamma-ray:

   (a) Leptonic process:
    The gamma-ray emission is produced by inverse Comptom scattering of the ISRF by CRe.

   (b) Hadronic process:
    In the hadronic model, CRp undergo hadronic collisions with thermal gas protons and produce γ-ray via pion decay. The volume emissivity of the emission can be written as

$$\epsilon \propto U_{\mathrm{CRp}} n_p \sigma_p \kappa_{pp}. \tag{10}$$

Note that the observed X-ray emission is contributed by all the gas in the Milky Way halo, which likely extends to a radius of ~250 kpc (Blitz & Robishaw 2000; Grcevich & Putman 2009), much bigger than our simulation box. Therefore, we first compute the X-ray emissivity from the simulated gas within a radius of 25 kpc away from the GC. Then, beyond 25 kpc the gas is assumed to be isothermal with $T = 10^6$ K and follows out to a radius of 250 kpc the observed density profile of (Tepper-García et al. 2015).

Inverse Compton scattering

$$\frac{dE}{dtd\epsilon_1 dV} = \frac{3}{4}\sigma_T c C \epsilon_1 \int_{\epsilon_{\min}}^{\epsilon_{\max}} \frac{n(\epsilon)}{\epsilon} d\epsilon \int_{\gamma_{\min}(\epsilon)}^{\gamma_{\max}} \gamma^{-(p+2)} f(q,\Gamma) d\gamma. \tag{11}$$

$$f(\gamma_{\mathrm{e}}, \epsilon) = 2q \ln q + (1+2q)(1-q) + 0.5(1-q)\frac{(\Gamma q)^2}{1+\Gamma q}, \tag{12}$$

$$\Gamma = \frac{4\epsilon\gamma_{\mathrm{e}}}{m_{\mathrm{e}}c^2} \tag{13}$$

$\gamma_{\min}(\epsilon)$ is the root of $f(\gamma_{\mathrm{e}}, \epsilon) = 0$ at a specific incident photon energy.

$$q = \frac{\epsilon_1/\gamma_{\mathrm{e}} m_{\mathrm{e}} c^2}{\Gamma(1 - \epsilon_1/\gamma_{\mathrm{e}} m_{\mathrm{e}} c^2)}. \tag{14}$$

Hadronic process

$$\frac{dE}{dtd\epsilon_1 dV} = cn_H pC\left(\frac{\epsilon_1}{m_{\mathrm{p}}c^2}\right)^{-p} \int_0^1 \sigma(\epsilon_{\mathrm{p}})F(x,\epsilon_{\mathrm{p}})x^p dx. \tag{15}$$

$$\sigma(\epsilon_{\mathrm{p}}) = 34.3 + 1.88L + 0.25L^2 \left[1 - \frac{E_{\mathrm{threshold}}}{E_{\mathrm{p}}}\right]^4 \mathrm{mb}. \tag{16}$$

$$F(x,\epsilon_{\mathrm{p}}) = B\frac{d}{dx}\left[\ln(x)\left(\frac{1-x^\beta}{1+kx^\beta(1-x^\beta)}\right)^4\right], \tag{17}$$

where $x = \epsilon_1/\epsilon_{\mathrm{p}}$, $B = 1.30 + 0.14L + 0.011L^2$, $\beta = \left(1.79 + 0.11L + 0.008L^2\right)^{-1}$, $\left(0.801 + 0.049L + 0.014L^2\right)^{-1}$, $L = \ln\left(\epsilon_{\mathrm{p}}/1 \text{ TeV}\right)$.

3. TO-DO-LIST

1. Predict cold inner bubbles, emitting OIII or OII spectrum.

4. CONCLUSIONS

DATA AVAILABILITY

The data underlying this article are available in the article and in its online supplementary material.

REFERENCES

Arnaud K. A., 1996, in Jacoby G. H., Barnes J., eds, Astronomical Society of the Pacific Conference Series Vol. 101, Astronomical Data Analysis Software and Systems V. p. 17

Bland-Hawthorn J., Gerhard O., 2016, Annual Review of Astronomy and Astrophysics, 54, 529

Blitz L., Robishaw T., 2000,] 10.1086/309457, 541, 675

Ferrière K. M., 2001, Rev. Mod. Phys., 73, 1031

Grcevich J., Putman M. E., 2009,] 10.1088/0004-637x/696/1/385, 696, 385

Johnston K. V., Spergel D. N., Hernquist L., 1995, The Astrophysical Journal, 451, 598

Kaastra J. S., Mewe R., 1993, A&AS, 97, 443

Lewis G. M., Austin P. H., 2002, 1th Conference on AtmosphericRadiation

Liedahl D. A., Osterheld A. L., Goldstein W. H., 1995, ApJL, 438, L115

Mathews W. G., 1971, ApJ, 165, 147

Mewe R., Gronenschild E. H. B. M., van den Oord G. H. J., 1985, A&AS, 62, 197

Miller M. J., Bregman J. N., 2013, The Astrophysical Journal, 770, 118

Schive H.-Y., Tsai Y.-C., Chiueh T., 2010, The Astrophysical Journal Supplement Series, 186, 457

Schive H.-Y., ZuHone J. A., Goldbaum N. J., Turk M. J., Gaspari M., Cheng C.-Y., 2018, Monthly Notices of the Royal Astronomical Society, 481, 4815

Snowden S. L., Cox D. P., McCammon D., Sanders W. T., 1990, The Astrophysical Journal, 354, 211

Synge J. L., 1957, North-Holland Pub. Co.; Interscience Publishers

Taub A. H., 1948, Physical Review, 74, 328

Tepper-García T., Bland-Hawthorn J., Sutherland R. S., 2015, The Astrophysical Journal, 813, 94

Tseng P.-H., Schive H.-Y., Chiueh T., 2021, Monthly Notices of the Royal Astronomical Society, 504, 3298

Valenti E., et al., 2018, A&AS, 616, A83

Wagner A. Y., Bicknell G. V., Umemura M., 2012, The Astrophysical Journal, 757, 136

Yang H.-Y. K., Ruszkowski M., Ricker P. M., Zweibel E., Lee D., 2012, The Astrophysical Journal, 761, 185

Yang H.-Y. K., Ruszkowski M., Zweibel E., 2013, Monthly Notices of the Royal Astronomical Society, 436, 2734

APPENDIX